Binary collision of CMAS droplets—Part I: Equal-sized droplets

Himakar Ganti[1,a)], Prashant Khare[1,b)], Luis Bravo[2]

[1]*Department of Aerospace Engineering, University of Cincinnati, Cincinnati, Ohio 45221-0070, USA*
[2]*Vehicle Technology Directorate, Army Research Laboratory, Aberdeen Proving Ground, Maryland 21005, USA*
a)Address all correspondence to these authors. e-mail: gantihr@mail.uc.edu
b)e-mail: prashant.khare@uc.edu

This study focuses on binary droplet collisions of equal calcium–magnesium–aluminosilicate (CMAS) droplets formed by the melting of dust and sand ingested by gas turbine engines. Head-on, off-center, and grazing collision of 1 mm CMAS droplets traveling toward each other at a relative velocity of 100 m/s are numerically investigated using a volume-of-fluid-based direct numerical simulation approach at operating pressure and temperature of 20 atm and 1548 K, respectively. It is found that head-on and off-center collisions lead to droplet coalescence, whereas stretching behavior is observed for the grazing configuration. To elucidate the effect of viscosity, a fictitious fluid with all properties the same as CMAS except for viscosity (1/10 of CMAS) is also studied. It is found that the lower viscosity liquid deforms significantly as compared to CMAS for the head-on and off-center cases. These differences are quantified using the budgets of kinetic, surface, and dissipation energies. This paper represents the first study of its kind on the binary collision of CMAS droplets.

Introduction

Rotorcraft gas turbine engines operating under environmentally degraded conditions (e.g., sandstorms, volcanic ash clouds, *etc.*) experience critical performance losses due to the ingestion of foreign matter particulates into the propulsion system. The most common types of ingested particulates range from volcanic ash to desert sand, to dust, or salt, in the form of molten particulates referred to as calcia–magnesia–alumino–silicates (CMAS) from here onwards, that often vary in composition depending on the geographical location. Although engine particle separator systems offer a potential solution to limit the amount of ingested contaminants, sufficiently smaller particles (<50 μm) mostly evade removal and are still entrained into the turbine stage [1]. The chamber temperatures of these engines have been increasing in the quest to improve efficiencies and thrust over the last few decades owing to substantial improvement in materials technologies, which has had an unintended consequence on ingested sand particles—they melt as they pass through the high-temperature combustor. The undesired entrainment of CMAS particulates and its evolution leads to multiple issues, including loss of efficiency and surge margin in the compressor, clogging of the fuel

spray nozzles in the combustor, and clogging of the nozzle vanes and cooling channels in the turbine hot section [2]. This, in turn, leads to rapid deterioration of material system components, increased maintenance, and the risk of critical loss of operation. To mitigate the detrimental effects of CMAS droplets deposited on the turbine blades, environmental- and thermal-barrier coatings (E/TBCs) along with film cooling of superalloy or ceramic matrix composites (CMC) components are used in today's engines to increase the durability of the materials. Without protective E/TBCs, the moisture in the combusting atmosphere will rapidly degrade the underlying substrate material due to the formation and volatilization of harmful gases [3]. Although T/EBCs are effective at its current capability of 2400 F, these strategies do not yet provide a robust solution to protect against increased CMAS attack at the ultimate goal of 3000 F (or higher temperatures), and as a result, still undergo severe degradation.

A necessary prerequisite to the development of effective TBCs is a thorough understanding of fundamental behaviors governing the interactions between CMAS droplets, while they are still in the combustion chamber, and subsequently, their interactions with the blade surface. While several research

cambridge.org/J

CrossMark

efforts have investigated the interactions between CMAS droplets and blade coatings, the associated deposition characteristics [2, 4, 5, 6, 7, 8, 9, 10, 11, 12, 13, 14, 15, 16, 17, 18], and the trajectories of particles in turbulent flowfield [19, 20], the limited literature exists on the phenomena dictating CMAS droplet–droplet interactions when they are still inside the combustion chamber. Knowledge of the droplet–droplet interaction outcomes is critically important to inform the development of deposition and accretion models of CMAS in the hot section. Therefore, the purpose of this paper is to elucidate the binary interactions between equal-sized CMAS droplets at operating pressure and temperatures representative of contemporary gas turbine combustion chambers.

Binary droplet collision for liquids, such as water and hydrocarbons relevant to propulsion applications, have been extensively studied in the past, and the detailed collision dynamics, atomization, and breakup regimes are fairly well established [21, 22, 23, 24, 25, 26, 27, 28, 29]. While the effect of viscosity on droplet collision has been studied in the past [30, 31, 32], CMAS viscosity and surface tension are at least two orders of magnitude higher than any liquid studied in the literature. Furthermore, there is wide uncertainty in CMAS physical properties, due to disparity in composition in different geographical regions, which will affect the fluid dynamic characteristics. Therefore, the behaviors of CMAS droplet collisions are expected to be very different as compared to previously investigated liquids [20].

To the best of our knowledge, no literature exists on the collision dynamics of CMAS droplets. This is primarily due to the challenges in making accurate measurements at temperatures corresponding to gas turbine combustion chamber conditions. It should be noted that at low temperatures, CMAS exists as a solid sand particle; therefore, CMAS droplet behaviors cannot be studied in ambient temperature conditions. This study aims to understand the process of binary collision of CMAS droplets in head-on and off-center configurations using high-fidelity Eulerian–Eulerian-based computational methodology. The current paper presents our investigation on equal-sized droplet collisions, and in a subsequent manuscript, we will discuss the collision outcomes of unequal CMAS droplets. To compare and contrast the role of CMAS viscosity, computations are also conducted on a fluid with the same physical properties as CMAS, except that the viscosity is reduced by one-tenth. The outcomes of this research will not only contribute to the collision physics of highly dense and viscous CMAS droplets but also provide estimates of the size distribution of droplets that will interact with turbine blades, which, in turn, determines the deposition characteristics.

The rest of the manuscript is organized into three major sections. In the next section, before discussing our results, we will describe the model validation and grid sensitivity analyses.

Next, we will discuss the physics associated with CMAS droplet collision in head-on, off-center, and grazing configurations. The quantitative analysis is based on the temporal evolution of surface, kinetic, and dissipation energies. This will be followed by the summary and conclusions that can be drawn from the research. In the last section, we will describe our methodology, including the governing equations, the numerical methods, and the grid adaptation technique used in this research effort.

Results and discussion

The results are organized into four subsections. First, we will describe relevant nondimensional numbers and the energies that will be used in our analysis. This will be followed by model validation and grid sensitivity studies. Finally, we will discuss CMAS collision physics both qualitatively using time evolution of the liquid volume fraction defined by $c = 0.5$, and quantitatively using the energy budget and the evolution of kinetic, surface, and viscous dissipation energies. We will also contrast CMAS droplet behaviors with a fictitious liquid with the same physical properties as CMAS except that the viscosity is one-tenth of it.

Relevant nomenclature, nondimensional numbers, and energies

The phenomenon of droplet collisions is described using Laplace number (La), droplet size ratio (Δ), and an impact parameter (B). Laplace number estimates the ratio of viscous forces to surface tension forces as

$$La = \left(\frac{We}{Re}\right), \qquad (1)$$

where We and Re are the Weber and Reynolds numbers, respectively. The droplet size ratio is defined as follows:

$$\Delta = \left(\frac{d_{small}}{d_{large}}\right). \qquad (2)$$

Figure 1 shows the geometric parameters relevant to binary droplet collision. The impact parameter B varies between 0 and 1, where 0 corresponds to head-on and 1 to grazing collision. B can be defined for droplets with different diameters D_1 and D_2, approaching each other with velocity U, and a projected separation χ, given by

$$B = \left(\frac{\chi}{R_1 + R_2}\right), \quad (R_1 \neq R_2);$$
$$B = \left(\frac{\chi}{2R}\right), \quad (R_1 = R_2). \qquad (3)$$

The results will be analyzed using the energy budget that consists of kinetic (KE), surface (SE), and dissipation (DE) energies, similar to the analysis conducted by other researchers
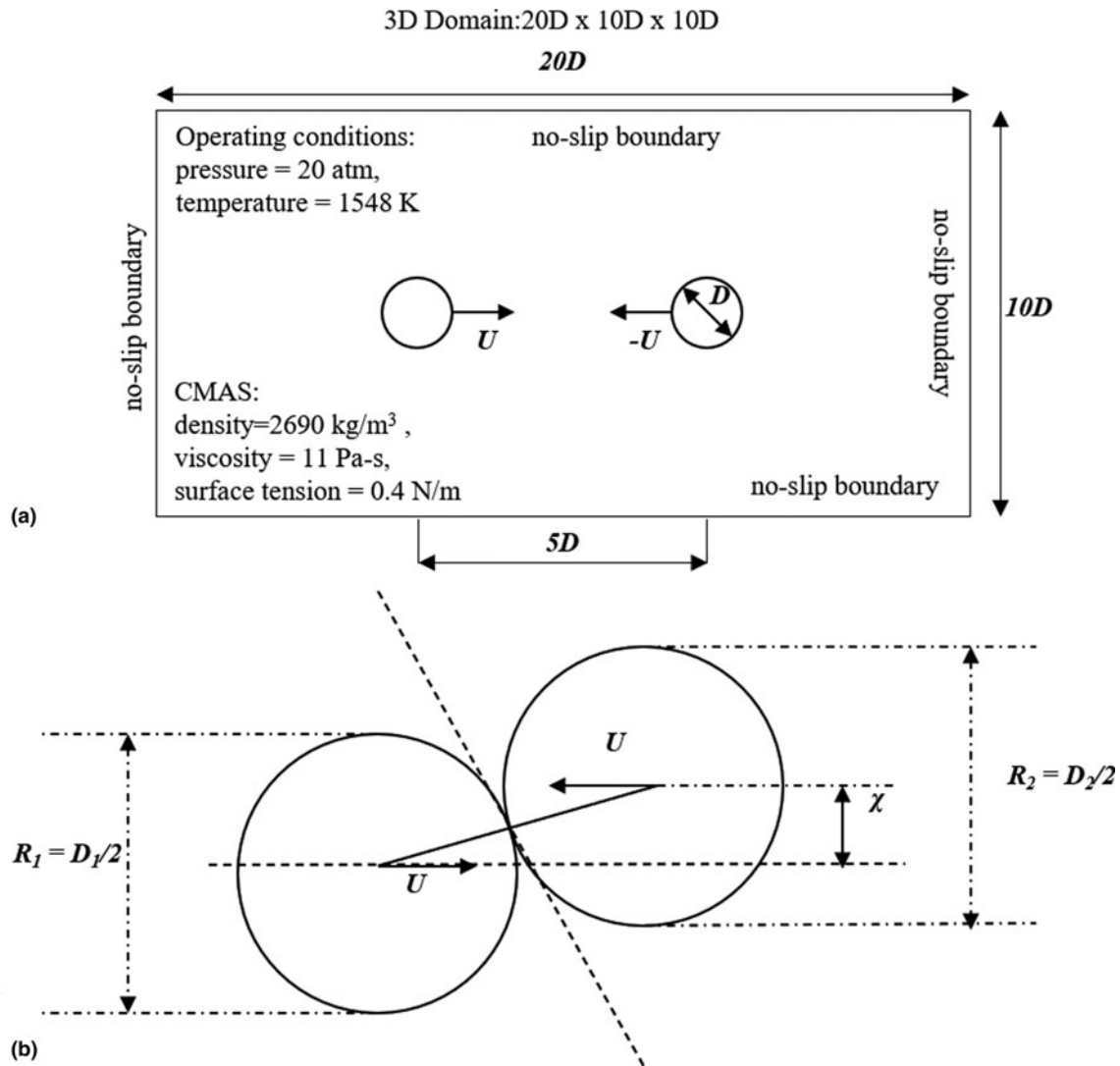
Figure 1: (a) Schematic of the computational setup and (b) relevant geometrical parameters governing droplet collision physics.

in the past [22, 29]. KE of the system is calculated using a volume-weighted sum of the liquid phase kinetic energy, whereas SE is calculated as the product of the surface tension and interfacial area. DE is defined as the time integral of the volume-weighted sum of the viscous deformation rate (VDR) given by [33, 34]

significantly high [28] which implies that reflexive or stretching separations that are responsible for the breakup of the liquid droplets after coalescence, will be restricted. It should be noted that since the energy equation is not explicitly solved in the current simulations, the sum of KE, SE, and DE will be defined as the total energy, TE. Later in

$$\text{VDR, } \Phi = \mu\left[2\left(\frac{\partial u}{\partial x}\right)^2 + 2\left(\frac{\partial v}{\partial y}\right)^2 + 2\left(\frac{\partial w}{\partial z}\right)^2 + \left(\frac{\partial v}{\partial x} + \frac{\partial u}{\partial y}\right)^2 + \left(\frac{\partial w}{\partial y} + \frac{\partial v}{\partial z}\right)^2 + \left(\frac{\partial u}{\partial z} + \frac{\partial w}{\partial x}\right)^2\right] + \lambda\left(\frac{\partial u}{\partial x} + \frac{\partial v}{\partial y} + \frac{\partial w}{\partial z}\right)^2. \quad (4)$$

Here, μ is the viscosity of the liquid phase and λ, based on Stokes' hypothesis, is $-2/3\mu$. For very high Laplace numbers, such as the current study, VDR is expected to be

the results section, the discussion will be based on KE, SE, and DE normalized by the maximum TE during the process.

Physical properties of CMAS and computational setup

The computational domain consists of 20D x 10D x 10D, where D is the diameter of the droplet (equal in this manuscript). All the numerical calculations are conducted at a pressure of 20 atm and temperature of 1548 K, conditions representative of a gas turbine combustor. At these conditions, the viscosity and density of air are 5.165×10^{-4} N s/m^2, and 4.56 kg/m^3, respectively. At these conditions, the physical properties of CMAS consist of [20] density, $\rho_{CMAS} = 2690$ kg/m^3; surface tension between CMAS/air, $\sigma_{CMAS} = 0.40$ N/m; and viscosity, $\mu_{CMAS} = 11.0$ N s/m^2. Based on guidance from the work by Bravo et al. [19], two droplets of diameter 1 mm are given a velocity of 50 m/s in the opposite direction for each case studied in this research. To elucidate the effect of viscosity, droplet collision of a fictitious fluid with the same properties as CMAS except for viscosity that is lowered by a factor of 10 is also studied. The Laplace numbers corresponding to CMAS and the fictitious fluid droplet collision are 112.45 and 1.12, respectively.

Computational challenges, model validation, and grid sensitivity analysis

Irrespective of the numerical method, the challenges accompanying numerical simulation of incompressible two-phase systems increase dramatically as the density ratio increases [35, 36]. The time integration scheme used in the current approach involves a classical time-splitting projection method, which requires the solution of the Poisson equation to obtain the pressure field:

$$\nabla \cdot \left[\frac{\Delta t}{\rho_{n+\frac{1}{2}}} \nabla p_{n+\frac{1}{2}} \right] = \nabla \cdot u_*. \quad (5)$$

Equation (5) is solved using a standard multigrid V-cycle methodology, and for large density and viscosity ratios, its solution suffers from slow convergence rates. One of the ways to overcome this issue is by using high grid resolution to resolve the steep density and viscosity gradients at the interface to ensure consistency in the momentum equation. Another method of speeding up the convergence rate is to spatially filter the interface during reconstruction. Even though the current methodology performs very well for the current configuration of droplet interaction at high viscosity and density ratios, the convergence can seriously degrade, depending on the problem and interface topology [37], in comparison with other methods [38]. Therefore, for all the cases conducted as a part of this research effort, including the validation study described in the next section, we have used both the aforementioned strategies to ensure accuracy: high grid resolution and spatially filtering (at least once) to ensure numerical accuracy and adequate resolution of the gas–liquid interface.

As a first step, grid sensitivity analysis is conducted to ensure appropriate grid resolution and is used to resolve the physics under consideration. The canonical configuration of equal CMAS droplets colliding head-on ($B = 0.0$) is selected for the grid sensitivity study. Figure 2 shows a comparison of the liquid morphology for four different refinement levels described below:

(i) level 6 at liquid/gas interface, level 5 for the droplet interior, and level 3 for the rest of the domain—L6.

(ii) level 7 at liquid/gas interface, level 6 for the droplet interior, and level 3 for the rest of the domain—L7.

(iii) level 8 at liquid/gas interface, level 7 for the droplet interior, and level 4 for the rest of the domain—L8.

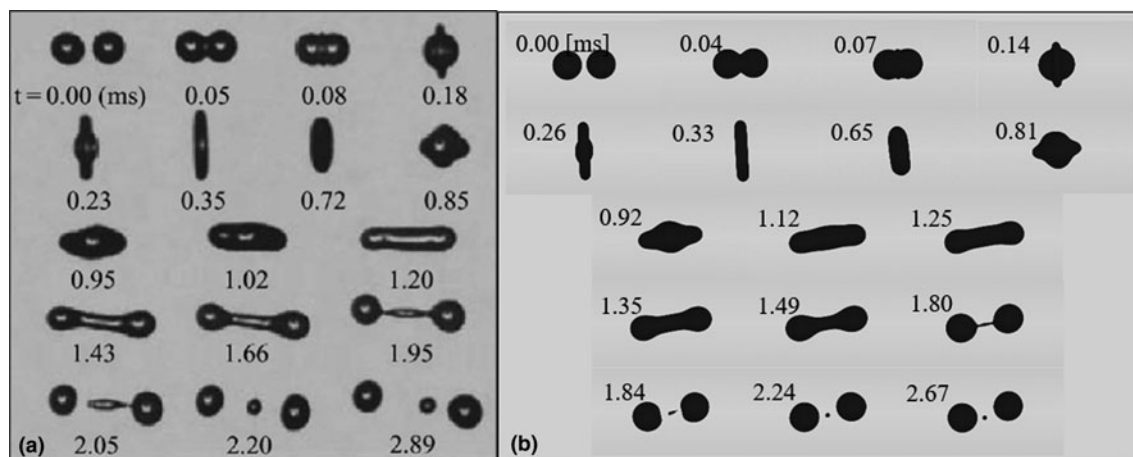(iv) level 9 at liquid/gas interface, level 8 for the droplet interior, and level 5 for the rest of the domain—L9.

Figure 2: Time evolution of the liquid interface when two tetradecane droplets collide at an impact factor, B = 0.06. (a) Experimental images of Qian and Law [21] shown on the left and (b) results from current simulations.

As seen clearly, L6 is unable to refine the interface sufficiently. While L7 resolves the interface better to ensure that the gas film when the droplets come closer to each other is resolved, L8 and L9 were investigated, which show almost identical results for interface deformation and evolution as well as the gas film. Therefore, for this study, L8 was selected as the grid resolution. While for high Weber number droplet collision, such as the current study, bouncing is not expected to be an outcome, in addition to gradient and value-based refinements, distance-based refinement is employed to ensure that the gas film is resolved accurately.

Next, model validation is conducted by simulating the experiments conducted by Qian and Law [21]. It should be noted that since no study in the past has investigated CMAS droplet collision, we have to resort to using data on tetradecane droplet collision for validation purposes. We chose a case that incorporates merging, retracting, and formation of satellite droplets to ensure that our framework can accurately model different aspects of the droplet collision phenomena. In this experiment, conducted at a pressure of 1 atm and 300 K, two droplets of diameter 336 μm with 2.48 m/s collide. The density and viscosity of air at these conditions are 1.18 kg/m^3 and $1.79 \times 10^{-4} \text{ N s/m}^2$, and that of tetradecane is 785.88 kg/m^3 and $2.21 \times 10^{-3} \text{ N s/m}^2$, respectively. The surface tension between tetradecane and air is 0.02656 N/m. Figure 3 shows the time evolution of events that take place as these droplets collide. The left side shows the experimental measurements and the right are results from the current simulation, showing excellent comparison. All flow features, including droplet coalescence, ligament formation and elongation, subsequent separation by pinching, and satellite droplet formation are accurately captured.

CMAS droplet collision

In the next few sections, we will discuss the dynamics of binary droplet collision for CMAS and the fluid that has a viscosity one-tenth that of CMAS. As mentioned before, the quantitative analysis is based on the energy budget that consists of kinetic, surface, and dissipation energies. The discussion will be based on the normalized values of these energies.

Head-on collision (B = 0.00)

Figure 1(a) shows the schematic of the computational setup. Two CMAS droplets of 1 mm diameter, separated by a distance of 5 mm are given equal and opposite velocities of 50 m/s. The corresponding La number is 112.45. Figures 4(a) and 4(b) show the time evolution of the front and side views, respectively, of this phenomenon. As the droplets travel toward each other, no apparent deformation is observed because of the high surface tension and viscosity. This is also confirmed quantitatively by looking at the surface energy plot in Fig. 6(a) that remains horizontal until the droplets come in contact with each other at $T = 0.3$. As the droplets come closer, a gas film is developed between them. However, since the relative velocity is quite high (100 m/s), the inertial forces overcome this air cushion, expelling it tangentially to the droplet motion, and come in contact with each other. This is followed by deformation and the development of a tangential contact plane leading to the eventual merging of the two droplets. A toroidal ridge is formed along the tangential plane, resulting in the formation of two rounded mushroom caps. These caps expand radially outward along the tangential plane after initial contact, as shown in the side view in Fig. 4(b). The reflexive movement within the larger droplet is severely restricted due to surface tension and high viscosity of CMAS. This leads to a gradual deformation of the resulting drop that stabilizes a short time after impact. These features are also reflected in the surface energy, shown in Fig. 6(a) which increases after the initial contact between the droplets and reaches a stationary state after a short time. Features such as a toroidal rim, extrusion disc, and surface instabilities that have been observed for high Weber number collisions in the literature [24, 25] are not observed as any perturbations and surface phenomena are damped
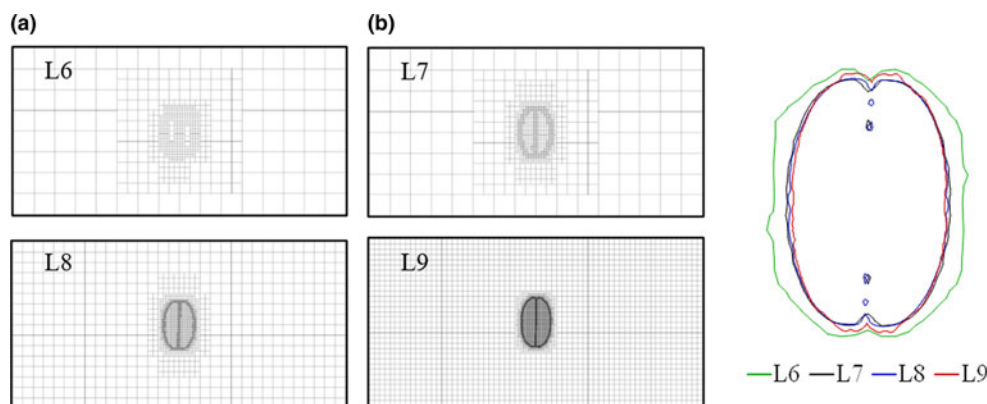

Figure 3: Grid sensitivity study based on levels 6, 7, 8, and 9. (b) shows an overlay of the liquid interface for these levels.[21].
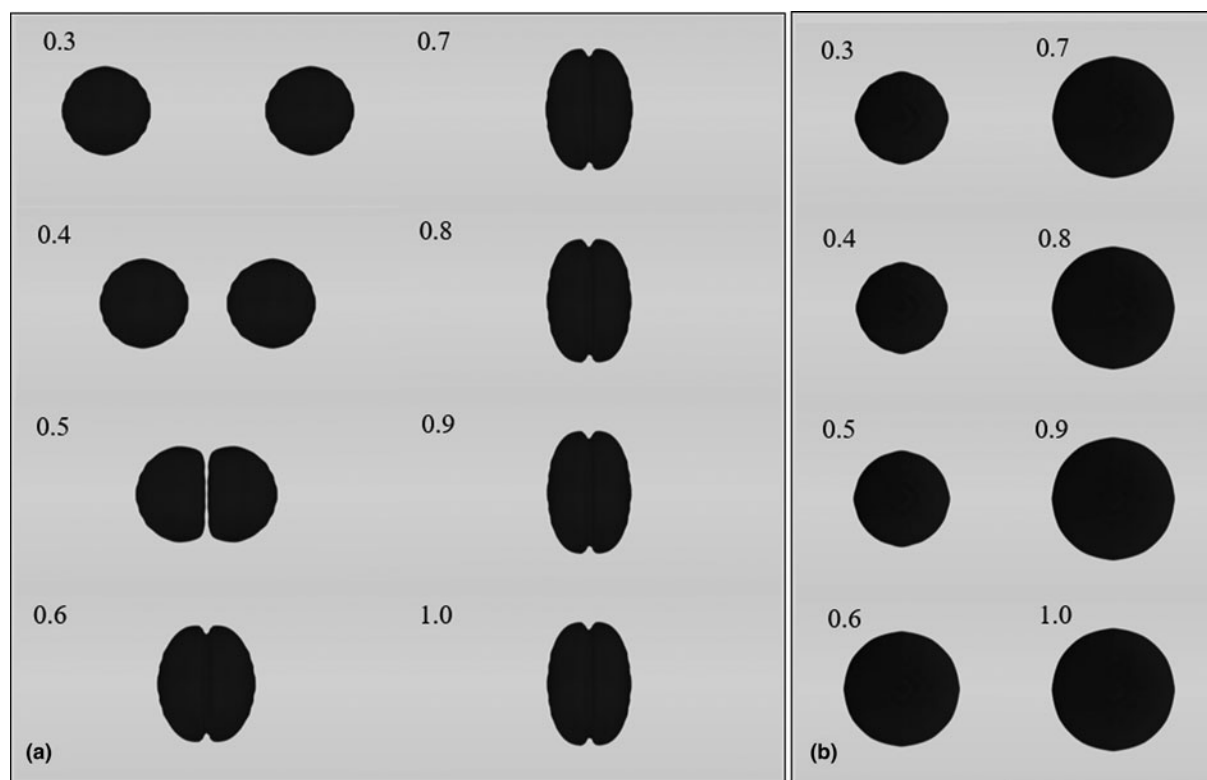
Figure 4: Time evolution of the liquid interface when two CMAS droplets collide at an impact factor, $B = 0$. (a) front view and (b) side view. Nondimensional time $T = t/(D/U)$.

because of high viscosity and surface tension of CMAS. The overall outcome is the coalescence of both droplets into a larger stationary drop with the formation of a toroidal ridge along the merging plane.

In contrast, as the droplets with one-tenth the viscosity of CMAS (referred to as $\mu_{CMAS/10}$) approach each other, they form a radially expanding extrusion disc that gets shattered due to fingering and ligamentation forming multiple smaller droplets, as shown in Figs. 5(a) and 5(b). Since this fluid has the same density and velocity as that of CMAS, it expels the gas film similar to the previous case, but because of lower viscosity, the inertia of the droplets leads to significant deformation followed by the breakup of the merging droplets. Since viscosity is much lower, after the droplets merge, the resulting droplet keeps deforming radially outwards and creates a thin sheet—this growth is observed in the front and side views in Fig. 5 from $T = 0.6–1.0$. As this sheet grows thinner, a toroidal Taylor–Culick rim and the extrusion disc with Rayleigh Plateau type instabilities are formed. These features have been observed by other researchers in the past [24, 25]. The disc is subjected to rapid thinning followed by lamellar destabilization leading to ligamentation with complete shattering into smaller droplets. Because of the formation of many droplets the surface energy increases significantly, as seen in the energy budget in Fig. 6(b).

These smaller droplets have a radially outward velocity component on the tangential plane and retain part of the initial KE.

In general, as the droplets move and collide, the exchange of energy takes place between KE, SE, and DE. Figure 6(a) shows the energy budget for CMAS droplet collision described in the previous section. As the CMAS droplets move toward each other, because of the high surface tension, there is little to no deformation, reflected by no change in surface energy till $T = 0.3$. During this time, because of the high viscosity, the viscous dissipation rate (VDR), calculated using Eq. (4), and consequently, DE (time integral of viscous dissipation energy) increases steadily. As these viscous droplets come in contact with each other ($T = 0.3–0.9$), there is a significant decrease in KE and an increase in SE corresponding to an increase in surface area. Simultaneously, the DE increases at a much higher rate because of the merging of highly viscous CMAS droplets. In contrast, for the fictitious liquid ($\mu_{CMAS/10}$), after the droplets collide, significant deformation takes place because of the lower viscosity, as observed by the evolution of SE in Fig. 6(b). VDR spikes at the time of impact, followed by a rapid decrease. SE has a small reduction at impact when the droplets star merging, owing to a small reduction in the surface area.
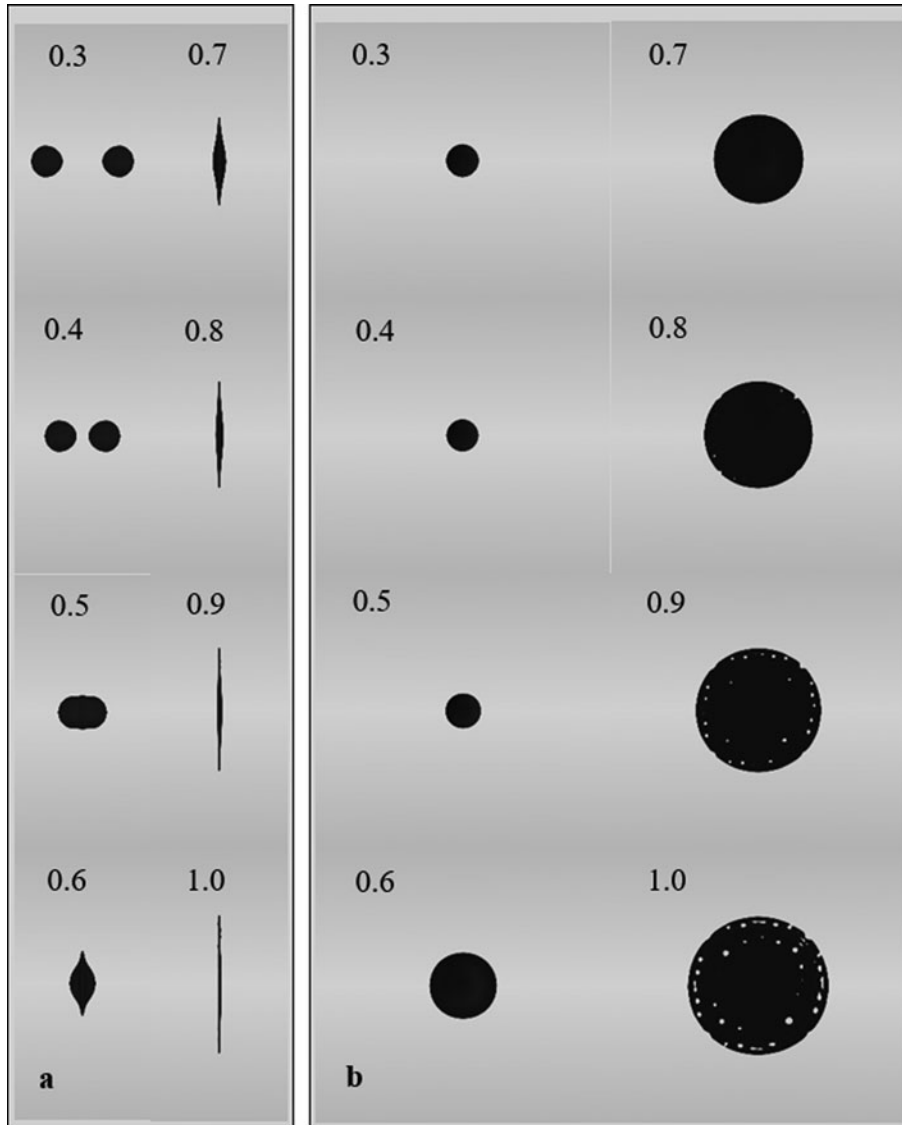
Figure 5: Time evolution of the liquid interface when two $\mu_{CMAS/10}$ droplets collide at an impact factor, $B = 0$. (a) front view and (b) side view. Nondimensional time $T = t/(D/U)$.
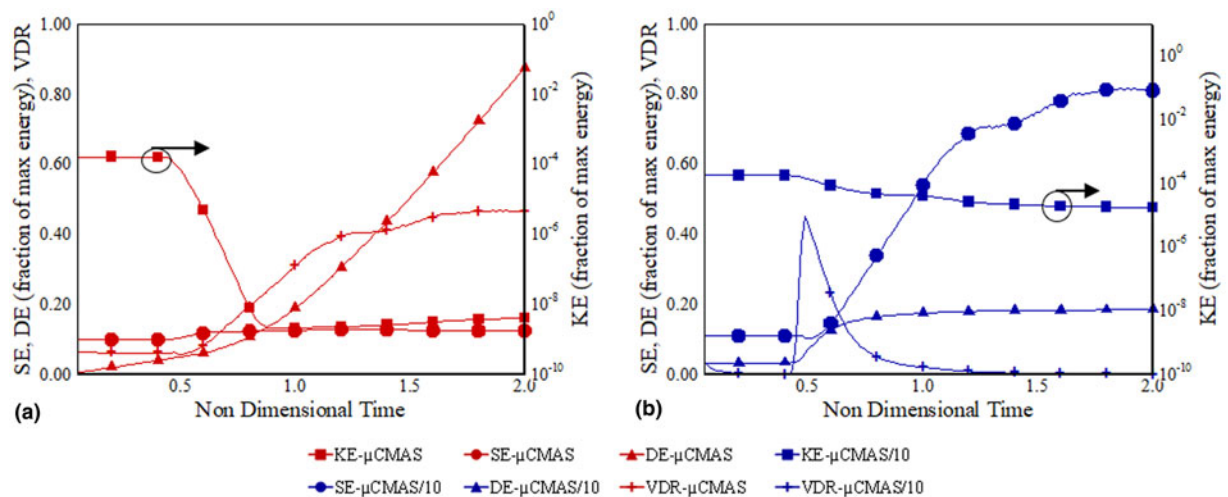

Figure 6: Time evolution of kinetic, surface, dissipation, and viscous dissipation rate for droplet collision at $B = 0$ for (a) CMAS droplets and (b) droplets with one-tenth the viscosity of CMAS.
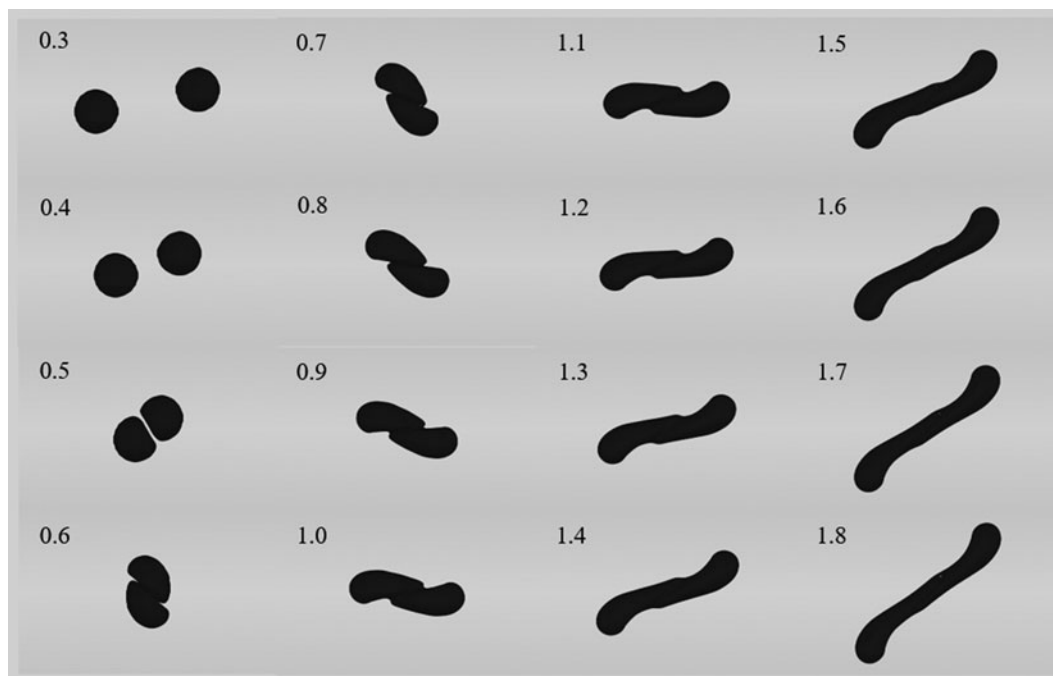
Figure 7: Time evolution of the liquid interface when two CMAS droplets collide off-center at an impact factor, $B = 0.5$. Nondimensional time $T = t/(D/U)$.

Off-center collision ($B = 0.50$)

Figure 7 shows the time evolution of the liquid interface for the off-center collision of CMAS droplets. The operating conditions, including the droplet velocities, are identical to the head-on collision case. For this case, as the CMAS droplets impinge on each other, they slide and deform along the tangential plane and transform into a hemispherical shape. Because of the high inertia of these droplets, their momentum keeps them moving. Simultaneously, the surface tension and viscous forces that are acting at the contact point result in the adhesion of these droplets as they try to slide. As a result, the momentum of the liquid at the contact point is lost, but the top and bottom droplet parts still try to move along the original direction, resulting in a torque causing rotational motion along an axis through the contact point and parallel to the tangential plane. The merged structure stretches until all momentum is lost and the droplet can no longer stretch, as observed from $T = 1.6–1.8$ in Fig. 7. Stretching separation is not observed because of high viscosity; however, the surface area continuously increases due to stretching of the resulting structure. These trends are also observed in the energy budget shown in Fig. 10(a), which in general are similar to that of the head-on collision, except that the SE, in this case, increases because of stretching.

As shown in Fig. 8(a), the initial events as droplets of the fictitious liquid ($\mu_{CMAS/10}$) approach each other are similar to that of CMAS—they deform along the tangential plane and form hemispherical bulges as the momentum of the droplets

moves them apart. Because the surface tension of these droplets is the same as CMAS (which is very high as compared to most liquids that are studied in the literature), they adhere to each other; however, since the viscosity is one-tenth of CMAS, there is stretching during the deformation process along the tangential plane. The bulk of the mass in the merged droplet is at the ends which through deformation and stretching creates a rim at the ends, and a sheet in the middle along the tangential plane. As stretching continues, the sheet becomes thinner and form fingers, as seen at $T = 1.4–1.8$ in Fig. 8(a). If we take a look at the side view at $T = 2.0$, shown in Fig. 8(b), breakup behaviors similar to beads-on-a-string are observed. These characteristics have been observed in the literature for droplet breakup of shear thinning non-Newtonian and very viscous droplets [39]. The energy budget for the off-center collision of lower viscosity liquid is very similar to that of the head-on collision case, except that the kinetic energy is retained throughout the process because of the continuous stretching of the merged structure. These trends are quantitatively shown in Fig. 10(b).

Grazing collision ($B = 0.80$)

Figure 9(a) shows the time evolution of the liquid interface when two CMAS droplets undergo collision, corresponding to $B = 0.8$. Similar to the off-center collision at $B = 0.5$, the droplets come in contact with each other tangentially and deform to form a tear-drop shaped lobe. However, since they are further apart along the horizontal axis, the surface tension
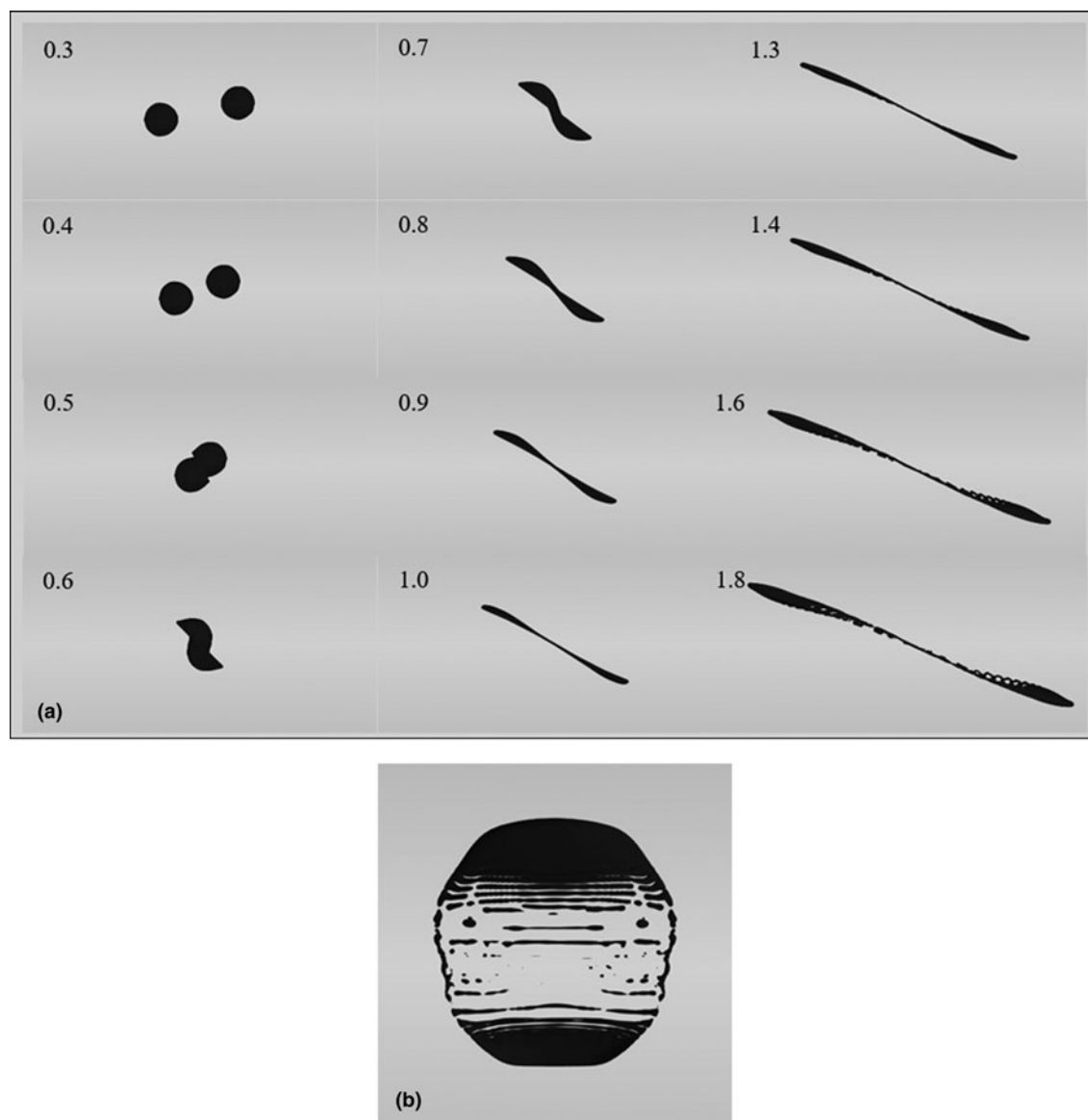
Figure 8: (a) Time evolution of the liquid interface when two $\mu_{CMAS/10}$ droplets collide off-center at an impact factor, $B = 0.5$ and (b) zoomed side view of the liquid interface at $T = 2.0$ showing beads-on-a-string type structures. Nondimensional time $T = t/(D/U)$.

acts at a much smaller contact area at the liquid–liquid interface. Two competing forces are acting on this two droplet system—the inertial force trying to maintain the momentum of the two droplets in opposite directions and the surface tension and viscous forces trying to merge the droplets. Different from the head-on and slightly off-center collision cases, the inertia dominates and instead of merging, the tear-shaped droplets maintain their motion and separate from each other with the creation of a satellite droplet. In addition to translational motion, because of their brief contact, slight rotation in the equal and opposite direction is imparted to the two droplets. The corresponding energy budget is shown in Fig. 10(c). As observed from the figure, there is a slight but progressive increase in the SE corresponding to the

formation and stretching of the tear-drop shape, and a monotonic decrease in KE as both the droplets dissipate energy to the air.

Figure 9(b) shows the time evolution of the liquid interface for the other liquid ($\mu_{CMAS/10}$). Similar to CMAS, the smaller contact area of the two droplets lead to the formation of lobes, which due to the higher malleability (due to lower viscosity) of this liquid leads to the formation of a thin lamellar central region. Since the bulk of the droplet mass does not interact, a significant fraction of momentum and KE is retained by the droplets. Unlike the CMAS droplets, for this fluid, the thin lamella at the contact surface stretches and eventually breaks up due to capillary instabilities. Breakup of the lamella leads to relaxation of the separating droplets that causes a
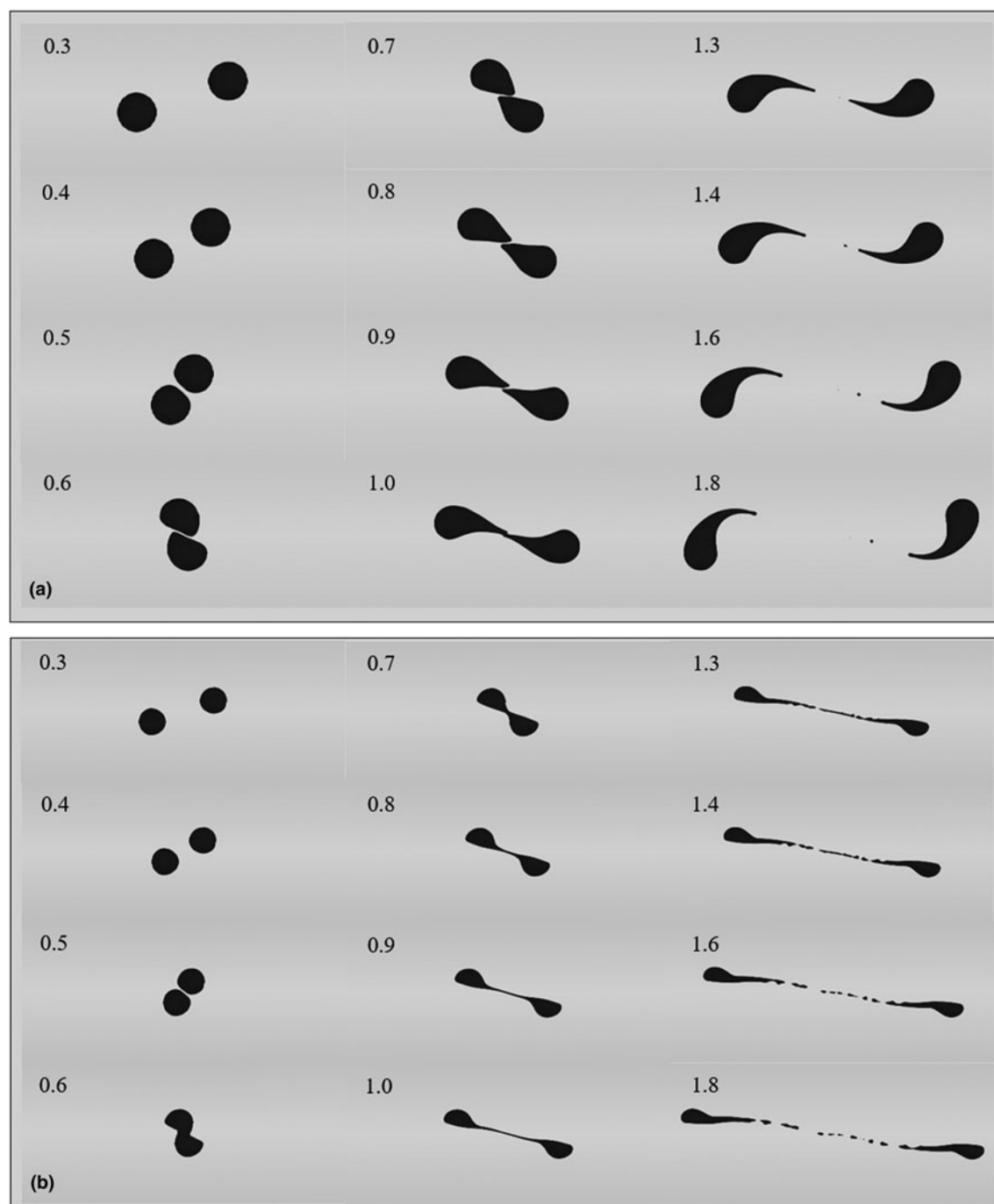
Figure 9: Time evolution of the liquid interface for grazing droplet collision at an impact factor, $B = 0.8$ for (a) CMAS droplets and (b) droplets with one-tenth the viscosity of CMAS. Nondimensional time $T = t/(D/U)$.

small decrease in the surface area, followed by an increase due to formation of satellite droplets. The energy budget is significantly different as compared to $B = 0.5$ case primarily because of the significantly reduced deformation for this case that leads to only a slight increase in SE. The DE increases slightly when the droplets interact, marked by the spike in VDR in the neighborhood of $T = 0.6$, after which it remains practically constant. KE maintains a constant fraction of the total energy for the

entire duration of the phenomena. These trends are shown in Fig. 10(d).

Summary

Collisions of equal-sized CMAS droplets ($\Delta = 1.0$) for three different impact parameters ($B = 0.0$, 0.5, and 0.8) were numerically simulated at conditions representative of a gas turbine
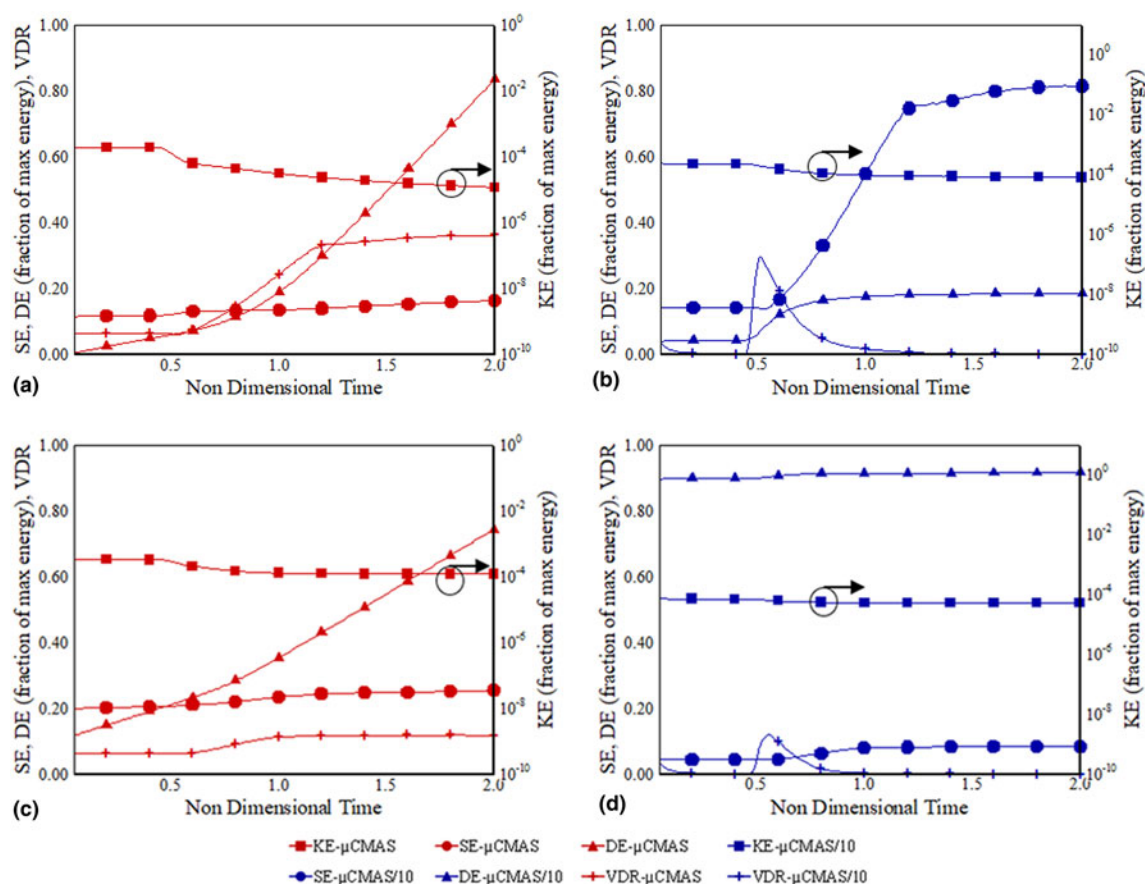
Figure 10: Time evolution of kinetic, surface, dissipation, and viscous dissipation rate for droplet collision for (a) CMAS droplets at $B = 0.5$; (b) droplets with one-tenth the viscosity of CMAS at $B = 0.5$; (c) CMAS droplets at $B = 0.8$; and (d) droplets with one-tenth the viscosity of CMAS at $B = 0.8$.

combustor to elucidate the fundamental processes and mechanisms that dictate their interactions. CMAS is in liquid form at these conditions and, therefore, was modeled as a liquid with appropriate density, viscosity, and surface tension—these physical properties have been previously reported in the literature. To identify the effect of the high viscosity of CMAS (it should be noted that the surface tension and viscosity of CMAS are at least two orders of magnitude higher than most hydrocarbons), a fictitious fluid with all properties identical to CMAS except viscosity, which was reduced by a tenth, was also studied. The droplets are given an initial velocity of 50 m/s, as they approach each other either head-on or off-center. It is found that for $B = 0$ and 0.5, due to the high Laplace number, results in the coalescence of CMAS droplets; a pear shape in the former and a stretched rotating structure with lobes at the end in the latter. For the lower viscosity fluid, while the droplets coalesce for both these cases too, they stretch significantly, forming thin films/structures, and eventually break up due to pinch-off. Separation occurs for grazing case ($B = 0.8$) for both CMAS and the fictitious fluid, however, the mechanism leading to it are completely different. For CMAS, the droplets deform into angled tear-drop shapes and continue in their original direction

producing a satellite drop. In contrast, the collision of droplets of the fictitious fluid leads to the development of a bridge that stretches, rotates, and then separates creating several satellite droplets. The droplet collision physics was quantified using the evolution of the normalized kinetic, dissipation, and surface energies.

Methodology

Current research poses two stringent challenges that need to be addressed to quantitatively identify the underlying physical processes present when two CMAS droplets interact. The challenges are (i) the presence of multiple phases and frequent interfacial topology changes and (ii) the existence of widely disparate length and time scales that need to be resolved in an accurate and computationally efficient manner. To accurately address the first issue, the most appropriate approach to investigating the flow physics of interest with high fidelity is based on a Eulerian–Eulerian framework, that is, all relevant phases (liquid and gaseous) being treated as continuous, and the interface between them is captured. This approach is also called the one-fluid approach in the literature [40]. To appropriately

resolve the wide range of spatial and temporal scales, an adaptive mesh refinement (AMR) methodology is adopted such that high resolution is achieved in reasonable turnaround time. Based on this rationale, the next subsection details the theoretical framework and numerical methods that are used in this research effort.

Governing equations

The formulation is based on the three-dimensional, incompressible, variable density form of the Navier–Stokes equations with surface tension. The mass conservation equation is given by

$$\frac{\partial \rho}{\partial t} + \vec{u} \cdot \nabla \rho = 0 \tag{6}$$

which, considering incompressibility becomes

$$\overrightarrow{\nabla \cdot u} = 0. \tag{7}$$

Conservation of momentum is given as

$$\frac{\partial \rho \vec{u}}{\partial t} + \nabla \cdot (\rho \vec{u} \vec{u}) = -\nabla p + \nabla \cdot \tilde{\tau} + \vec{F}_{st}, \tag{8}$$

where F_{st} is the surface tension force per unit volume and τ is the shear stress tensor.

$$\tilde{\tau} = \mu(\nabla \vec{u} + (\nabla \vec{u})^T). \tag{9}$$

A state-of-the-art, high-resolution, VOF) interface capturing method is adopted for large-scale interfacial evolution. Surface tension is accommodated as a Dirac distribution function on the interface. Governing equations are written in a Eulerian reference frame to capture the gas–liquid interface. A VOF scalar variable c, to trace the multi-fluid interface is given as follows:

$$c = \begin{cases} 0, & \text{fluid 1} \\ 1, & \text{fluid 2} \end{cases} \tag{10}$$

Density and viscosity for each computational cell are defined as linear functions of c as follows:

$$\begin{aligned} \rho(c) &= c\rho_1 + (1-c)\rho_2, \\ \mu(c) &= c\mu_1 + (1-c)\mu_2. \end{aligned} \tag{11}$$

The advection equation for density can then be written as an equivalent equation for the volume fraction:

$$\frac{\partial c}{\partial t} + (\vec{u} \cdot \nabla c) = 0. \tag{12}$$

The conservation equations are written for the different phases without using the jump condition at the interface, which translates to singularities in the governing equations. It

can be shown that this formulation is equivalent to that written for each phase separately with the pressure jump condition at the interface. As pointed out by Tryggvason et al. [40], the one-fluid approach can be interpreted in two ways, in a weak sense, in which the governing equations are satisfied only in the integral form, or by admitting solutions using step and delta functions. In this study, we use the latter approach by modeling the surface tension effects using the continuum surface force model developed by Brackbill et al. [41]:

$$\vec{F}_{st}(\vec{x}_1) = \sigma \int_S \kappa(\vec{x}_2)\hat{n}(\vec{x}_2)\delta(\vec{x}_1 - \vec{x}_2)dS, \tag{13}$$

where σ is the surface tension force, κ is the local curvature, and δ is the Dirac delta function. κ is evaluated as follows:

$$\kappa = \frac{1}{R_1} + \frac{1}{R_2}, \tag{14}$$

where R_1 and R_2 are the principal radii of curvature. Surface tension force for each cell at the interface is approximated by

$$\vec{F}_{st} \approx \sigma \kappa \delta \hat{n}. \tag{15}$$

Numerical approach and mesh adaptation

The governing equations described above are solved using a projection method based on variable density fractional step numerical methodology using a Gerris framework [37, 42]. The interim velocity is computed in the first step. The pressure field is then computed by solving the Poisson equation and projecting the interim velocity onto a divergence-free velocity field. Quad/octree spatial discretization is used in combination with a multigrid V-cycle Poisson solver to obtain the pressure distribution. The primitive variables, such as momentum components, pressure, and volume fraction, are volume averaged and collocated at the cell centers of the discretized volume. This collocated definition of primitive variables is useful for mesh adaptation and facilitates the implementation of the Godunov scheme for the nonlinear convective terms. To treat the viscous terms accurately, an approximate projection method developed by Almgren et al. [43] is used. The scalar VOF variable c is obtained by solving the advection equation for the volume fraction. A piecewise-linear geometrical VOF scheme generalized for quad/octree spatial discretization is used to solve Eq. (7). The value of c in each cell then corresponds to the fraction of the finite volumes filled with different phases. Computational cells completely filled with fluid 1 are characterized by $c = 0$ and fluid 2 by $c = 1$, and cells containing the interface are characterized by $0 < c < 1$. Since face-centered velocities are divergence-free, and the function c is then advected using the computed velocity field. Details of the various numerical algorithms used in this paper can be found elsewhere [37, 42, 44].

Even though fixed mesh algorithms have been used successfully for dynamically evolving interfacial flows, it is extremely computationally expensive and often cost-prohibitive. AMR is one of the most efficient ways to mitigate this problem. The AMR implementation used in the present research is based on structured grids to facilitate the implementation of the various numerical algorithms and reduce the computational overhead while providing excellent mass conservation characteristics. The octree discretization further assists in the implementation of the multigrid V-cycle solver for the solution of the Poisson equation. The structured adaptive mesh refinement (SAMR) grid methods have been successfully used by researchers to explore a wide range of physical phenomena, ranging from large-scale numerical relativity to fluid dynamics and combustion simulations [45, 46, 47, 48].

Therefore, to ensure that the wide range of spatial and temporal scales are resolved with high fidelity, an AMR technique is implemented to improve the solution accuracy and efficiency. The adaptive quad/octree spatial discretization is especially useful for the liquid–gas and liquid–liquid interface refinement. The grid adaptation criterion depends on physics under consideration. Several refinement criteria, including value, gradient, distance, and thickness based are implemented to resolve the interfacial and interior characteristics of the CMAS droplet collision phenomena. The grid is refined or coarsened by comparing the refinement indicator in each cell to a predefined threshold value. Further, the code is parallelized based on message passing interface libraries for massively parallel computations. This framework has been used extensively for a wide range of multiphase flow problems, including liquid jet atomization in the presence of broadband inlet fluctuations, impinging liquid jets, droplet breakup, and collision phenomena [29, 49, 50, 51].

Various numerical schemes used for the spatial discretization impose restrictions on the maximum allowable time step that can be used to ensure numerical stability. These constraints are determined by the convective, viscous, and surface tension terms, and the time step is calculated based on the following criteria:

Convective term: this constraint is probably the most well-known and is defined by the Courant Friedrichs and Lewy (CFL) condition given by the following equation:

$$\mathbf{max}\left[\frac{|u_{i,j,k}|\Delta t_{\text{convection}}}{\Delta}\right] < \text{CFL}_{\text{max}}. \tag{16}$$

This restriction ensures that the fluid volume convected to the neighboring cell is not more than the amount of fluid in the cell. We used a conservative value of 0.5 for the CFL number during our simulations to ensure consistency and accuracy.

Surface tension term: the stability condition for the explicit treatment of surface tension is restricted by the appropriate

time step resolution of the capillary waves given by [41]

$$\Delta t_{\text{st}} = \sqrt{\frac{\rho_L + \rho_g}{4\pi\sigma}\Delta^3}. \tag{17}$$

Viscous term: the time step restriction imposed by this term is given by

$$\Delta t_{\text{visc}} = \min\left[\frac{\rho(c)_{i,j,k}}{\mu(c)_{i,j,k}}\frac{\Delta^2}{6}\right]. \tag{18}$$

The time step chosen for a given instant is given by the minimum of these three times.

Acknowledgments

References

1. **A. Filippone and N. Bojdo**: Turboshaft engine air particle separation. *Prog. Aerosp. Sci.* **46**, 224–245 (2010).

2. **M. Murugan, A. Ghoshal, A. Nieto, M. Walock, L. Bravo, N. Jain, M. Pepi, J. Swab, D. Zhu, R.T. Pegg, C. Rowe, A. Flatau, and K. Kerner**: Prevention of molten sand attack on thermal barrier coatings for rotorcraft gas turbine blades – A round Robin test evaluation. In *Annual Forum Proceedings* (AHS International, Fairfax, VA, USA, 2018).

3. **D.K. Larry Fehrenbacher, J. Kutsch, I. Vesnovsky, E. Fehrenbacher, A. Ghoshal, M. Walock, M. Murugan, and A. Nieto**: Advanced environmental barrier coatings for SiC CMCs. In *Advances in Ceramics for Environmental, Functional, Structural, and Energy Applications II*, Vol. **266**. M.M. Mahmoud, K. Sridharan, H. Colorado, A.S. Bhalla, J.P. Singh, S. Gupta, J. Langhorn, A. Jitianu, and N. Jose Manjooran, eds (John Wiley & Sons, Hoboken, NJ, USA, 2019); pp. 83–93.

4. **A. Ghoshal, M. Murugan, M.J. Walock, A. Nieto, L. Bravo, B. Barnett, M. Pepi, C. Hoffmeister Mock, J. Swab, and S. Hirsch**: Sandphobic coatings and surface modification of hot section components of next generation VTOL engines: Current and future research efforts. In *Forum, Joint Propulsion Conference, Cincinnati, OH USA* (AIAA, Reston, VA, USA, 2018); p. 4831.

5. **S. M. Whitaker and J. P. Bons**: An improved particle impact model by accounting for rate of strain and stochastic rebound. In *Proceedings of ASME Turbo Expo (IGTI), Oslo, Norway* (ASME, New York, NY, USA, 2018).

6. **K. Yu and D. Tafti**: Size- and temperature-dependent collision and deposition model for micron-sized sand particles. *J. Turbomach.* **141**, 031001-1–031001-11 (2019).

7. **W. Song, S. Yang, M. Fukumoto, Y. Lavallée, S. Lokachari, H. Guo, Y. You, and D.B. Dingwell**: Impact interaction of in-flight high-energy molten volcanic ash droplets with jet engines. *Acta Mater.* **171**, 119–131 (2019).

8. **S. Singh and D. Tafti**: Particle deposition model for particulate flows at high temperatures in gas turbine components. *Int. J. Heat Fluid Flow* **52**, 72–83 (2015).

9. **D. Pearson and R. Brooker**: The accumulation of molten volcanic ash in jet engines: Simulating the role of magma composition, ash particle size and thermal barrier coatings. *J. Volcanol. Geotherm. Res.* **389**, 106707 (2020).

10. **N. Libertowski, N. Plewacki, and J.P. Bons**: The effect of temperature and melting relative to particle deposition in gas turbines. In *AIAA Scitech 2019 Forum, Jan 7 to 11, San Diego, CA, USA* (American Institute of Aeronautics and Astronautics, Reston, VA, USA, 2019).

11. **K. Hsu, B. Barker, B. Varney, A. Boulanger, V. Nguyen, and W.F. Ng**: Review of heated sand particle deposition models. In *Proceedings of ASME Turbo Expo (IGTI), Oslo, Norway* (ASME, New York, NY, USA, 2018).

12. **A. Guha**: Transport and deposition of particles in turbulent and laminar flow. *Annu. Rev. Fluid Mech.* **40**, 311–341 (2008).

13. **E.D. Crowe and J.P. Bons**: Effects of dust composition on particle deposition in an effusion cooling geometry. In *Proceedings of ASME Turbo Expo (IGTI), Phoenix, AZ, USA* (ASME, New York, NY, USA, 2019).

14. **J.P. Bons, R. Prenter, and S. Whitaker**: A simple physics-based model for particle rebound and deposition in turbomachinery. *J. Turbomach.* **139**, 081009-1–081009-12 (2017).

15. **N. Bojdo, M. Ellis, A. Filippone, M. Jones, and A. Pawley**: Particle-Vane interaction probability in gas turbine engines. *J. Turbomach.* **141**, 091010-1–091010-13 (2019).

16. **M. Murugan, A. Ghoshal, M.J. Walock, B.D. Barnett, M.S. Pepi, and K.A. Kerner**: Sand particle-induced deterioration of thermal barrier coatings on gas turbine blades. *Adv. Aircr. Spacecr. Sci.* **4**, 37–52 (2017).

17. **M. Murugan, A. Ghoshal, M. Walock, A. Nieto, L. Bravo, B. Barnett, M. Pepi, J. Swab, R.T. Pegg, C. Rowe, D. Zhu, and K. Kerner**: Microstructure based materials and particulate interactions and assessment of coatings for high temperature turbine blades. In *Proceedings of ASME Turbo Expo (IGTI), Charlotte, NC USA* (ASME, New York, NY, USA, 2017).

18. **A. Ghoshal, M. Murugan, M.J. Walock, A. Nieto, B.D. Barnett, M.S. Pepi, J.J. Swab, D. Zhu, K.A. Kerner, C.R. Rowe, C.Y. Shiao, D.A. Hopkins, and G.A. Gazonas**: Molten particulate impact on tailored thermal barrier coatings for gas turbine engine. *J. Eng. Gas Turbines Power* **140** (2018).

19. **L.G. Bravo, Q. Xue, M. Murugan, A. Ghoshal, M. Walock, and A. Flatau**: Particle transport analysis of sand ingestion in gas turbine jet engines. In *53rd AIAA/SAE/ASEE Joint Propulsion Conference, Jul 10 to Jul 12, Atlanta, GA, USA* (AIAA, Reston, VA, USA, 2017); pp. 1–14

20. **N. Jain, L. Bravo, S. Bose, D. Kim, M. Murugan, A. Ghoshal, and A. Flatau**: Turbulent multiphase flow and particle deposition of sand ingestion for high-temperature turbine blades. In *Proceedings of the Summer Program, Jun 24 to Jul 20, Stanford, CA, USA* (Center for Turbulence Research, Stanford, CA, USA, 2018); pp. 35–44.

21. **J. Qian and C.K. Law**: Regimes of coalescence and separation in droplet collision. *J. Fluid Mech.* **331**, 59–80 (1997).

22. **K.-L. Pan, C.K. Law, and B. Zhou**: Experimental and mechanistic description of merging and bouncing in head-on binary droplet collision. *J. Appl. Phys.* **103**, 064901 (2008).

23. **M.R. Nobari, Y.J. Jan, and G. Tryggvason**: Head-on collision of drops—A numerical investigation. *Phys. Fluids* **8**, 29–42 (1996).

24. **M. Liu and D. Bothe**: Numerical study of head-on droplet collisions at high weber numbers. *J. Fluid Mech.* **789**, 785–805 (2016).

25. **C.-K. Kuan, K.-L. Pan, and W. Shyy**: Study on high-Weber-number droplet collision by a parallel, adaptive interface-tracking method. *J. Fluid Mech.* **759**, 104–133 (2014).

26. **X. Jia, J.-C. Yang, J. Zhang, and M.-J. Ni**: An experimental investigation on the collision outcomes of binary liquid metal droplets. *Int. J. Multiphase Flow* **116**, 80–90 (2019).

27. **X. Chen, D. Ma, P. Khare, and V. Yang**: Energy and mass transfer during binary droplet collision. In *49th AIAA Aerospace Sciences Meeting including the New Horizons Forum and Aerospace Exposition* (American Institute of Aeronautics and Astronautics: Orlando, FL, USA, 2011); pp. 1–17.

28. **N. Ashgriz and J.Y. Poo**: Coalescence and separation in binary collisions of liquid drops. *J. Fluid Mech.* **221**, 183–204 (1990).

29. **X. Chen, D. Ma, P. Khare, and V. Yang**: Energy and mass transfer during binary droplet collision. In *49th AIAA Aerospace Sciences Meeting including the New Horizons Forum and Aerospace Exposition, Jan 4 to Jan 7, Orlando, FL, USA* (AIAA, Reston, VA, USA, 2011); pp. 1–14.

30. **C. Gotaas, P. Havelka, H.A. Jakobsen, H.F. Svendsen, M. Hase, N. Roth, and B. Weigand**: Effect of viscosity on droplet-droplet collision outcome: Experimental study and numerical comparison. *Phys. Fluids* **19**, 102106 (2007).

31. **C. Focke and D. Bothe**: Direct numerical simulation of binary off-center collisions of shear thinning droplets at high Weber numbers. *Phys. Fluids* **24**, 073105 (2012).

32. **M. Sommerfeld and M. Kuschel**: Modelling droplet collision outcomes for different substances and viscosities. *Exp. Fluids* **57**, 187 (2016).

33. **I.M. Cohen, P.K. Kundu, and D.R. Dowling**: *Fluid Mechanics*, 5th ed. (Academic Press, Waltham, MA, USA, 2012).

34. **F. White**. *Viscous Fluid Flow*, 3rd ed. (McGraw Hill, New York, NY, USA, 2006).

35. **O. Desjardins and V. Moureau**: Methods for multiphase flows with high density ratio. In *Proceedings of the Summer Program, Jun 27 to Jul 23, Stanford, CA, USA* (Center for Turbulence Research, Stanford, CA, USA, 2010); pp. 313–322.

36. **M. Gorokhovski and M. Herrmann**: Modeling primary atomization. *Ann. Rev. Fluid Mech.* **40**, 343–366 (2008).

37. **S. Popinet**: An accurate adaptive solver for surface-tension-driven interfacial flows. *J. Comput. Phys.* **228**, 5838–5866 (2009).

38. **D. Gerlach, G. Tomar, G. Biswas, and F. Durst**: Comparison of volume-of-fluid methods for surface tension-dominant two-phase flows. *Int. J. Heat Mass Transfer* **49**, 740–754 (2006).

39. **P. Khare and V. Yang**: Breakup of non-Newtonian liquid droplets. In *44th AIAA Fluid Dynamics Conference, Jan 16 to Jan 20, Atlanta, GA, USA* (AIAA, Reston, VA, USA, 2014).

40. **G. Tryggvason, R. Scardovelli, and S. Zaleski**: *Direct Numerical Simulations of Gas-Liquid Multiphase Flows* (Cambridge University Press, New York, NY, USA, 2011).

41. **J.U.U. Brackbill, D.B.B. Kothe, and C. Zemach**: A continuum method for modeling surface tension. *J. Comput. Phys.* **100**, 335–354 (1992).

42. **S. Popinet**: Gerris: A tree-based adaptive solver for the incompressible Euler equations in complex geometries. *J. Comput. Phys.* **190**, 572–600 (2003).

43. **A.S. Almgren, J.B. Bell, and W.Y. Crutchfield**: Approximate projection methods: Part I. inviscid analysis. *SIAM J. Sci. Comput.* **22**, 1139–1159 (2000).

44. **P. Khare**: Breakup of liquid droplets. Ph.D. thesis, Georgia Institute of Technology, Atlanta, GA, USA, 2014.

45. **J. Bell**: AMR for low Mach number reacting flow. In *Adaptive Mesh Refinement – Theory and Applications*. Lecture Notes in Computational Science and Engineering, vol **41**. T. Plewa, T. Linde, and V. Gregory Weirs, eds (Springer, Berlin, Heidelberg, Germany, 2006); pp. 203–221.

46. **H. Jourdren**: HERA: A hydrodynamic AMR platform for multiphysics simulations. In *Adaptive Mesh Refinement – Theory and Applications*. Lecture Notes in Computational Science and Engineering, vol **41**. T. Plewa, T. Linde, and V. Gregory Weirs, eds (Springer, Berlin, Heidelberg, Germany, 2006); pp. 283–294.

47. **C.R. Myers**: The dynamics of localized coherent structures and the role of adaptive software in multiscale modeling. In *Structured Adaptive Mesh Refinement (SAMR) Grid Methods*, S.B. Baden, N.P. Chrisochoides, D.B. Gannon, and M.L. Norman, eds (Springer, New York, NY, USA, 2000); pp. 111–125.

48. **M. Pernice, M.J. Bockelie, D. Swensen, and P.J. Smith**: Progress, results, and experiences in developing an adaptive solver for steady state turbulent reacting flows in industrial boilers and furnaces. In *Structured Adaptive Mesh Refinement (SAMR) Grid Methods*, S.B. Baden, N.P. Chrisochoides, D.B. Gannon, and M.L. Norman, eds (Springer, New York, NY, USA, 2000); pp. 127–151.

49. **J. Gamertsfelder, P. Khare, and L.G. Bravo**: Investigation of atomization behaviour of liquid monopropellants in pintle injectors. In *Proceedings of ASME Turbo Expo (IGTI) 2020, June 22-26, London, England* (ASME, New York, NY, USA, 2020).

50. **V. Notaro, P. Khare, and J.G. Lee**: Mixing characteristics of non-Newtonian impinging jets at elevated pressures. *Flow Turbul. Combust.* **102**, 355–372 (2019).

51. **D.-J. Ma, X.-D. Chen, P. Khare, and V. Yang**: Atomization patterns and breakup characteristics of liquid sheets formed by two impinging jets. In *49th AIAA Aerospace Sciences Meeting Including the New Horizons Forum and Aerospace Exposition, Jan 4 to Jan 7, Orlando, FL, USA* (AIAA, Reston, VA, USA, 2011); pp. 2011–2097.